Instrument-model refinement in normalised reciprocal-vector space for X-ray Laue diffraction

Radosław Kamiński,[a,*] Dariusz Szarejko,[a] Martin N. Pedersen,[b] Lauren E. Hatcher,[c,d] Piotr Łaski,[a] Paul R. Raithby,[c] Michael Wulff,[e] Katarzyna N. Jarzembska [a,*]

[a] Department of Chemistry, University of Warsaw, Żwirki i Wigury 101, 02-089 Warsaw, Poland

[b] Niels Bohr Institute, University of Copenhagen, Universitetsparken 5, 2100 Copenhagen, Denmark

[c] Department of Chemistry, University of Bath, Claverton Down, Bath, BA2 7AY, United Kingdom

[d] School of Chemistry, Cardiff University, Main Building, Park Place, Cardiff, CF10 3AT, United Kingdom

[e] European Synchrotron Radiation Facility, 71 avenue des Martyrs, 38043 Grenoble, France

* Corresponding authors: Radosław Kamiński (rkaminski85@uw.edu.pl)
Katarzyna N. Jarzembska (katarzyna.jarzembska@uw.edu.pl)

Abstract: A simple yet efficient instrument-model refinement method for X-ray diffraction data is presented and discussed. The method is based on least-squares minimisation of differences between respective normalised (*i.e.* unit length) reciprocal vectors computed for adjacent frames. The approach was primarily designed to work with synchrotron X-ray Laue diffraction data collected for small-molecule single-crystal samples. We have shown the method works well on both simulated and experimental data. Tests performed on simulated data sets for small-molecule and protein crystals confirmed the validity of the proposed instrument-model refinement approach. Finally, examination of exemplary data sets collected at both BioCARS 14-ID-B (Advanced Photon Source) and ID09 (European Synchrotron Radiation Facility) beamlines indicated that our approach is capable of retrieving goniometer parameters (*e.g.* detector distance or primary X-ray beam centre) reliably, even when their initial estimates are rather inaccurate.

Synopsis: Diffractometer instrument-model refinement method for X-ray Laue data is presented and tested. It is shown the approach works well even when the initial geometrical parameters deviate significantly from the target values.

Keywords: data processing, Laue diffraction, instrument model, refinement, X-ray diffraction

Table of Contents Graphic

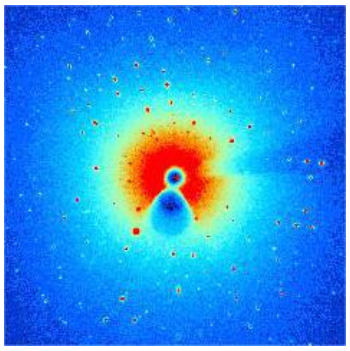

1. Introduction

Studies of short-lived light-induced excited states in crystals of small molecules are currently feasible almost exclusively at high-intensity X-ray sources, such as synchrotrons (Hatcher & Raithby, 2014, Coppens, 2011, Coppens *et al.*, 2010). In this regard, the time-resolved (TR) X-ray diffraction Laue method, applied originally for macromolecular samples (Ren *et al.*, 1999, Hajdu *et al.*, 1987), constitutes the most efficient approach, as it allows effectively single-pulse diffraction experiments thanks to a superb X-ray flux. However, it should be noted that data processing in the case of a polychromatic X-ray beam is considerably more difficult when compared to the monochromatic approach (Coppens & Fournier, 2015). Among other factors, this is caused by a number of wavelength-dependent corrections which have to be applied. Such problems can be significantly reduced by employing the so-called RATIO method (Coppens *et al.*, 2009), in which the Laue experiment provides only light-ON to light-OFF reflection intensity ratios ($I^{\mathrm{ON}}/I^{\mathrm{OFF}}$). These in turn are further analysed so as to achieve electron-density photodifference maps and later structural models of transient species (Trzop *et al.*, 2014, Jarzembska *et al.*, 2014, Makal *et al.*, 2012, Benedict *et al.*, 2011, Jarzembska *et al.*, 2019, Coppens *et al.*, 2017, Vorontsov *et al.*, 2010). Consequently, the data processing pipeline concentrates here on the integration of diffraction spots (Kalinowski *et al.*, 2012, Szarejko *et al.*, 2020) and crystal orientation-matrix determination. For small-molecule crystals the latter step is most efficiently achieved with the algorithm proposed by Kalinowski *et al.* (Kalinowski *et al.*, 2011) and implemented in the *LAUEUTIL* software. Nevertheless, the success of this approach depends heavily on a proper description of the used goniometer geometry, described with a mathematical instrument model (IM) including parameters of the experimental setup (*e.g.* detector distance, detector size and position, goniostat zeros *etc.*) (Paciorek *et al.*, 1999). Therefore, in more difficult cases, where sufficiently accurate instrument-model parameters are not available (an inaccurate IM is quite common on a busy, user-operated synchrotron beamline, where equipment is regularly moved or exchanged depending on different user requirements *etc.*), the entire data processing is significantly hampered (if it is possible at all), since the *LAUEUTIL* suite does not have capabilities either to determine or to refine the IM. Such option is provided, for example, in the *PRECOGNITION* suite (Šrajer *et al.*, 2000) which, however, is not open-source and is not fully optimised for small-molecule crystals where sparse diffraction patterns are observed. In such cases it requires the collection of a reference data set on a known protein crystal standard (*e.g.* photoactive yellow protein, PYP (Borgstahl *et al.*, 1995)) prior to actual experiments. In cases where such reference data is not available the

data processing is much more problematic. Hence, to fill-in this gap, in the current short contribution a simple yet efficient *ab initio* method to refine instrument-model parameters is reported. Importantly, the algorithm relies only on diffraction spot positions, and does not require an orientation-matrix, wavelength spectrum, *etc.*

2. Results and discussion

A typical Laue X-ray diffraction experiment performed for a single-crystal sample is depicted schematically in Figure 1*a*. Diffraction images (*i.e.* frames) are usually collected for a sample being kept still (*i.e.* not rotated during the exposure), since it is possible to record full reflections using a polychromatic X-ray beam. This feature of the method allows to employ it efficiently for time-resolved X-ray diffraction studies. In this contribution we assume the simplest case of a Laue experiment, in which a total of N frames (*e.g.* 90 or 180 frames) are collected during sample rotation along single-spindle axis, each at different sample orientation separated from the adjacent one by some angular interval, $\Delta\varphi$ (*e.g.* 1° or 2°). Figure 1*b* shows how the selected diffraction spots change positions on the detector surface when the crystal is rotated along horizontal axis. Furthermore, we assume that the sample is firmly attached to the holder (*e.g.* it is glued), thus no irregular sample movements are present.

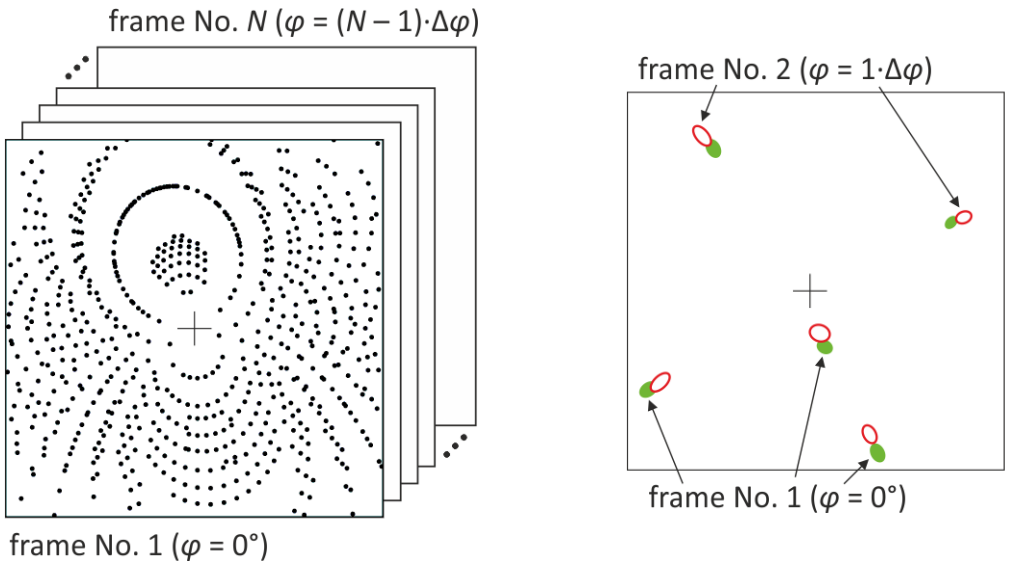

Figure 1. (*a*) Schematic representation of a typical Laue data set consisting of diffraction frames measured at various goniometer setting angles (*i.e.* each frame is collected with the sample rotated by a certain increment, $\Delta\varphi$; single φ-angle spindle axis is assumed for

simplicity; this example data set consists of N frames; cross indicates the frame's centre). (*b*) Overlay of two exemplary adjacent frames showing changes in positions of selected spots due to the horizontal sample rotation ($\Delta\varphi$ = 1°): green solid spots – frame No. 1, red empty spots – frame No. 2 (for overlay of two frames see the Supporting Information; displacements, spot sizes and shapes are exaggerated).

Since in the Laue method a polychromatic X-ray beam is diffracted by a single-crystal sample, assigning a specific wavelength to a given recorded single diffraction spot is not initially straightforward. Thus, before the orientation-matrix and indexing data processing steps, reconstruction of the reciprocal space is not feasible. (We note that such procedures are much easier when the unit cell parameters are *a priori* known, but become more cumbersome in the case of sparse diffraction patterns.) Nonetheless, it is possible to compute normalised (*i.e.* unit-length) reciprocal-space vectors, $\underset{\sim}{\mathbf{h}}$, as proposed by Kalinowski *et al.* (Kalinowski *et al.*, 2011):

$$\underset{\sim}{\mathbf{h}} = \frac{\mathbf{s} - \mathbf{s}_0}{\|\mathbf{s} - \mathbf{s}_0\|} \tag{1}$$

where $\mathbf{s}$ and $\mathbf{s}_0$ are the diffracted and primary beams unit-length vectors, respectively. The $\underset{\sim}{\mathbf{h}}$ vectors are subsequently appropriately rotated (using goniometer setting angles known for each frame) to a common goniometer-head-fixed coordinate system (with all goniometer angles equal zero), yielding a unit-sphere-projected set of vectors (denoted here as $\underset{\sim}{\mathbf{h}}_0$ for convenience) for the entire data set (for visualisation see, for example, Figure 1*b* in ref. (Kalinowski *et al.*, 2011)). Computation of the $\underset{\sim}{\mathbf{h}}_0$ vectors from spot positions on the detector surface requires knowledge of the instrument-model parameters, thus each vector of this kind is the function of those parameters (for details see the Supporting Information).

During the analysis of the available TR Laue data sets it appeared that, despite using an approximate IM parameters (*e.g.* detector distance is off by several millimetres), most of the $\underset{\sim}{\mathbf{h}}_0$ vectors computed for the reflection with the same hkl indices present in the adjacent frames are very similar one to another in terms of direction. For ideal IM parameters such derived $\underset{\sim}{\mathbf{h}}_0$ vectors should overlap (this is schematically shown in Figure 2, in which two selected pairs of $\underset{\sim}{\mathbf{h}}_0$ vectors computed for the adjacent frames are presented). This fact constitutes the basis for our refinement procedure. The $\underset{\sim}{\mathbf{h}}_0$ vectors computed for the adjacent frames are first paired using a simple geometrical criterion (*i.e.* the angular separation). The sum of difference vectors' lengths in these pairs,

$$S = \sum_{j=1}^{N-1} \sum_{k(j)} \left\| \underset{\sim}{\mathbf{h}}_{0,k,j} - \underset{\sim}{\mathbf{h}}_{0,k,j+1} \right\|^2 \qquad (2)$$

is then least-squares minimised with respect to the chosen instrument-model parameters (j and k denote frames and vector pairs found for two adjacent frames, respectively; j index runs from 1 to $N-1$, for data set with N frames; note that the number of determined reflection pairs is different for various pairs of adjacent frames), starting from some initial estimated values (*e.g.* an approximate detector distance).

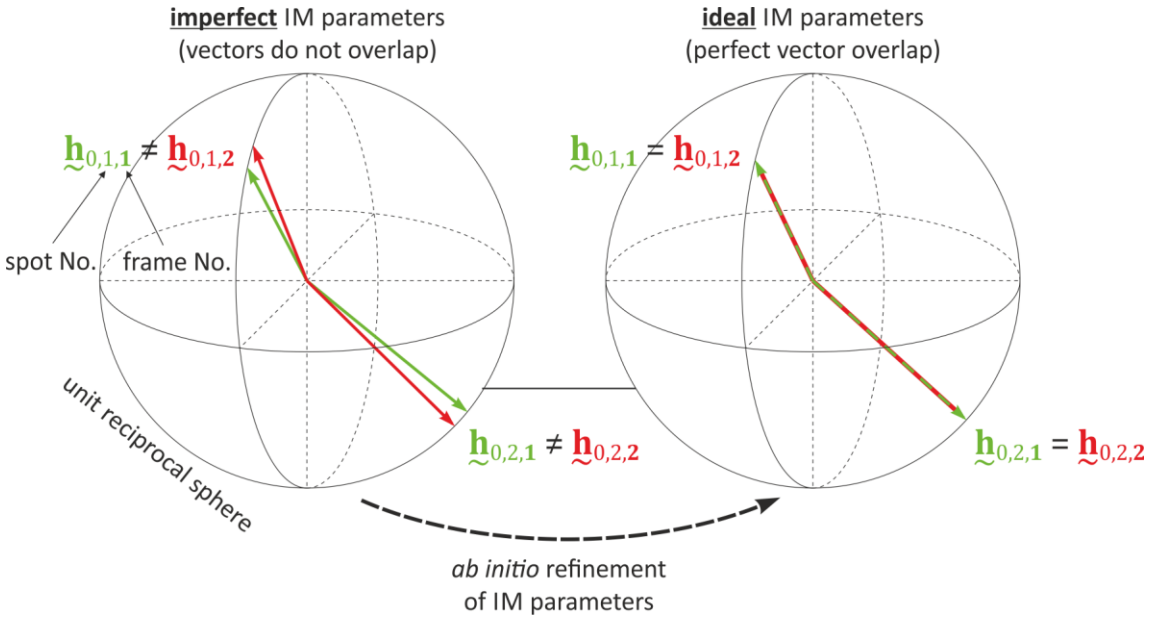

Figure 2. Schematic representation of two selected adjacent-frames' pairs of normalised reciprocal vectors $\underset{\sim}{\mathbf{h}}_0$ with the same hkl indices (for example see Figure 1*b*) reconstructed from spot positions, goniometer setting angles and other instrument model parameters (*e.g.* detector distance, primary beam position *etc.*). Left panel: imperfect IM parameters (the respective vectors do not overlap), right panel: ideal IM parameters (the reconstructed vectors overlap perfectly after the least-squares minimisation of vector differences with respect to IM parameters).

In our simple IM only three parameters are considered crucial for further data analysis with the RATIO method, namely the detector distance, the horizontal and vertical primary beam position on the detector surface: d, x_0 and y_0, respectively. It is assumed that the detector is placed ideally perpendicularly at 2θ = 0° with respect to the primary beam and there are no further goniometer misalignments. More details on the instrument model, used

definitions, equations, and implementation comments are available in the Supporting Information.

The algorithm was tested on a couple of model simulated and experimental data sets. The refinement of the instrument model on simulated X-ray Laue diffraction data sets for two crystal structures, *i.e.* of a small-molecule compound, $Ag_2Cu_2L_4$ (L = 2-diphenylphosphino-3-methylindole) (Koshevoy *et al.*, 2011), and a pea lectin protein (Einspahr *et al.*, 1986) constituted the primary benchmark. The silver(I)-copper(I) tetranuclear complex was studied by us using both TR Laue diffraction and high-pressure crystallography (triclinic space group $P\bar{1}$) (Jarzembska *et al.*, 2018, Jarzembska *et al.*, 2014). In turn, the second simulated data set was generated for the pea lectin protein crystal structure, which was studied extensively with Laue diffraction by Helliwell and co-workers (orthorhombic space group $P2_12_12_1$) (Cruickshank *et al.*, 1991, Helliwell *et al.*, 1989, Cruickshank *et al.*, 1987, Machin, 1985). It should be noted that the simulated models account only for the diffraction geometry and not diffraction spot intensities (for details see the Supporting Information). Instead, experimental data sets of excellent quality collected for two copper(I) complexes are used as two further test cases. The first one, Cu(dppe)(dmp)PF_6 (dppe = 1,2-bis(diphenylphosphino)ethane, dmp = 2,9-dimethyl-1,10-phenanthroline) (monoclinic space group $P2_1/c$), was studied previously by Voronstsov *et al.* (Vorontsov *et al.*, 2009) using the monochromatic TR technique and later by us using both Laue and in-house TR diffraction methods (Trzop *et al.*, 2014, Coppens *et al.*, 2016, Kaminski *et al.*, 2014). The data set used here was measured at the 14-ID-B BioCARS beamline (Graber *et al.*, 2011) at the Advanced Photon Source (APS). The data for the second compound, Cu(dppe)(dmdpp)PF_6 (dmdpp = 2,9-dimethyl-4,7-diphenyl-1,10-phenanthroline) (monoclinic space group $P2_1/n$), were collected at the ID09 beamline (Wulff *et al.*, 2002) at the European Synchrotron Radiation Facility (ESRF). It should be noted that both data sets were initially integrated using our new 1-dimentional seed-skewness method (Szarejko *et al.*, 2020), which resulted in a set of reflection intensities and positions. All data sets examined in this study are summarised in Table 1, including their abbreviations used hereafter. Exemplary simulated and experimental frames are shown in the Supporting Information.

Table 1. Selected parameters for simulated and experimental data sets used in this study.

Parameter	*Simulated data*		*Experimental data*	
Compound	$Ag_2Cu_2L_4$ complex	Pea lectin protein	Cu(dppe)(dmp) PF_6 complex	Cu(dppe)(dmdpp) PF_6 complex
Data set abbreviation	**simAgCu**	**simPeaL**	**expCuDppe**	**expCuDmdpp**
X-ray source	–	–	14-ID-B at APS	ID09 at ESRF
Space group	$P\bar{1}$ (No. 2)	$P2_12_12_1$ (No. 19) [£]	$P2_1/c$ (No. 14)	$P2_1/n$ (No. 14)
a / Å	12.6106(2)	50.73(2)	20.2099(4)	14.1511(6)
b / Å	14.1988(3)	61.16(2)	13.6740(3)	14.2212(5)
c / Å	22.0662(4)	136.59(8)	26.5809(5)	27.3870(10)
α / °	76.3912(3)	90	90	90
β / °	81.5811(3)	90	95.5178(2)	98.373(3)
γ / °	66.8814(3)	90	90	90
Detector distance, d / mm	65.0 [¶]	95.0 [¶]	100.0 [#]	50.0 [#]
Beam position,				
x_0 / pix	1954.0 [¶]	1215.0 [¶]	1986.0 [$]	1910.0 [&]
y_0 / pix	1973.0 [¶]	1286.0 [¶]	1964.0 [$]	1924.0 [&]
Detector shape	square	square	square [†]	square [‡]
Detector dimensions [¥] / mm	340.0	120.0 [§]	340.0 [†]	170.0 [‡]
Frame dimensions [¥] / pix	3840	2400 [§]	3840 [†]	3840 [‡]
Pixel size [¥] / μm	89.0	20.0 [§]	89.0 [†]	44.0 [‡]
Wavelength range				
$\lambda_{\min}$ / Å	0.8	0.5	0.8 [€]	0.75 [€]
$\lambda_{\max}$ / Å	1.1	2.6	1.1 [€]	1.1 [€]
Number of frames	91	91	91	91
Angular increment, $\Delta\phi$ / °	1.0	1.0	1.0	1.0
Angular coverage, ϕ_{tot} / °	91.0	91.0	91.0	91.0

[¥] Both dimensions (vertical and horizontal) are the same. [£] For simplicity systematic absences' conditions are omitted in this contribution. [¶] Values used in the simulation. [§] Parameters as close as possible to mimic the CEA reflex emulsion films (Helliwell *et al.*, 1989). [#] As assumed to be correct in the data collection software. [$] Primary beam position measured with the *ADXV* program (Arvai, 2019) from the reference frame with direct beam image (appropriate filters were used to maximally attenuate the beam). [&] Primary beam position was assumed to be close to the beamstop shadow centre. [†] Rayonix MX340-HS detector mounted at the 14-ID-B BioCARS beamline at APS (Graber *et al.*, 2011). [‡] Rayonix MX170-HS detector mounted at the ID09 beamline at ESRF (Wulff *et al.*, 2002). [€] Limiting values estimated from the λ-curve plots.

Results of the instrument-model refinement are shown in Table 2. In the case of simulated data, **simAgCu** and **simPeaL**, the refinements converge very well to the values used in the simulation with estimated standard deviations (e.s.d.s) in the order of 10^{-5} or better (in mm or pix), indicating a nearly perfect fit. It should be stressed that the correct results are obtained even if the detector distance deviates from the real value by more than 1 cm. Therefore, the achieved accuracy is far more than sufficient for real applications, as the initial detector distance can easily be determined to at least 1 mm precision with mechanical tools.

In turn, regarding the data collected at the 14-ID-B beamline at APS, **expCuDppe**, the instrument geometry was tested with the PYP crystal and *PRECOGNITION* software. The primary beam position was determined by collecting its direct image by attenuating X-rays,

therefore this data set can be used to test the accuracy of our software at reproducing these known parameters. In our software, refinement of the instrument parameters from different starting points (including the detector distance set to as much as 120 mm) yielded essentially identical results, *i.e.* d = 100.80(7) mm instead of the assumed exact value of 100 mm. We believe this is well within experimental error, thus such difference is perfectly acceptable. The beam position refined to values that are almost identical to those we measured when the detector was directly exposed to the attenuated primary beam.

In the second case of the **expCuDmdpp** data set, collected at the ID09 beamline of the ESRF, we encountered some problems when indexing the measured data using the method of Kalinowski *et al.* without any IM refinement. As such, this data set presented a challenge for our software. The final step of the indexing method is to cluster the points in the Euler-angle space, each representing a single determined orientation matrix (the method is based on testing multiple orientation matrices). The final orientation matrix is considered to be an average of all matrices belonging to a single cluster. For the ESRF data, the detector distance was initially set and calibrated to 50 mm. The detector centre was not directly measured, but instead it was assumed to be very close to the centre of the X-ray beamstop shadow area (x_0 = 1910 pix, y_0 = 1924 pix; see the Supporting Information). However, starting from these values the procedure yielded only 10 clusters for **expCuDmdpp**. This rather poor determination of the orientation matrix hampered considerably further data processing. We ascribe these difficulties to imperfect instrument-model parameters, which tend to drift from their starting positions (properly calibrated initially) over the very long experiment time (*ca.* 5 days of constant data collection). The refinement of the IM parameters (final values: d = 47.25(2) mm, x_0 = 1904.1507(9) pix, y_0 = 1923.046(1) pix) with our new approach enabled us to find the orientation matrix readily and reliably. The total number of determined clusters increased considerably (to 268), which indicated correct determination of the crystal orientation. It is also worth noting the refined beam centre stayed in the beamstop shadow area, which constituted additional confirmation of the IM refinement method's validity.

It appears that there are essentially no correlations between the refined parameters. The largest correlation coefficients, which reach only up to 20 %, are found for the simulated data sets (*ca.* 20% for x_0-y_0 parameter pair and *ca.* 18% for d-x_0, for **simAgCu** and **simPeaL**, respectively). In turn, correlation coefficients' values calculated for the experimental data sets do not exceed 6%. Such results can be expected, since in our method changes in the d, x_0 and y_0 parameters have significantly different effect on the reflections' positions and thus on the computed normalised vectors (change in d results in the radial movement of reflections – all

inwards or outwards, whereas changes in x_0 and y_0 lead to the reflections' vertical or horizontal shifts, respectively). We believe that larger correlations might be found when more elaborate and complex instrument models are implemented (*e.g.* incorporating goniometer angles' zeros, detector pitch-roll-yaw misalignment angles, *etc.*), or when other physical factors cannot be neglected during the data collection (*e.g.* laser-pulse-induced thermal expansion of a crystal may have somewhat similar effect on the diffraction pattern as the distance change). These, however, are not considered in this contribution.

Table 2. Refinement of selected parameters for the studied Laue data sets. Note d is expressed in mm, whereas x_0 and y_0 in native detector pixel coordinates (see the Supporting Information). In certain cases the errors are so small that a non-standard notation for values and their e.s.d.s are used.

Data set	*Initial values*			*Final values*		
	d	x_0	y_0	d	x_0	y_0
simAgCu¶	70.0	1954.0	1973.0	65.00 ± 8·10^{-5}	1954.00 ± 1·10^{-5}	1973.00 ± 2·10^{-5}
	65.0	1920.0	1973.0	65.00 ± 8·10^{-5}	1954.00 ± 1·10^{-5}	1973.00 ± 2·10^{-5}
	80.0	1920.0	1985.0	65.00 ± 8·10^{-5}	1954.00 ± 1·10^{-5}	1973.00 ± 1·10^{-5}
simPeaL $	105.0	1215.0	1286.0	95.00 ± 3·10^{-5}	1215.00 ± 1·10^{-6}	1286.00 ± 1·10^{-6}
	95.0	1240.0	1286.0	95.00 ± 3·10^{-5}	1215.00 ± 1·10^{-6}	1286.00 ± 1·10^{-6}
	100.0	1240.0	1250.0	95.00 ± 3·10^{-5}	1215.00 ± 1·10^{-6}	1286.00 ± 1·10^{-6}
expCuDppe ¥	120.0	1986.0	1964.0	100.80(7)	1986.174(5)	1965.013(7)
	100.0	1950.0	1964.0	100.80(7)	1986.174(5)	1965.013(7)
	120.0	1950.0	1950.0	100.80(7)	1986.177(5)	1965.020(7)
expCuDmdpp	50	1910	1924	47.25(2)	1904.1507(9)	1923.046(1)
	55	1900	1900	47.25(2)	1904.1497(9)	1923.044(1)
	70	1920	1950	47.25(2)	1904.1504(9)	1923.047(1)

¶ Target values for **simAgCu**: d = 65.0 mm, x_0 = 1954.0 pix, y_0 = 1973.0 pix (Table 1). $ Target values for **simPeaL**: d = 95.0 mm, x_0 = 1215.0 pix, y_0 = 1286.0 pix (Table 1). ¥ Target values for **expCuDppe**: d = 100.0 mm, x_0 = 1986.0 pix, y_0 = 1964.0 pix (Table 1).

Finally, it should be stressed that the main assumption of the method is that the crystal remains fixed during the entire experiment, thus any irregular movements during the data collection are eliminated. This is most efficiently realised by gluing the crystal to the capillary, which constitutes a standard practice for crystals of small molecules. Such sample handling is especially important during the time-resolved experiments where the high-power laser hits the sample and thus may change the crystal orientation. For small molecules, where the highest possible accuracy and precision is necessary, it is a crucial issue of the further data processing utilising the RATIO method. On the other hand, in the case of protein samples gluing of the crystal to a capillary is often impractical (it has not been done even in the case of

PYP which was successfully analysed with the modified RATIO method (Schotte *et al.*, 2012)). In consequence, here the crystal can move more significantly, which predominates slight goniometer misalignments. Taking into account the differences in the data processing techniques (protein diffraction patterns are much less sparse), these misalignments are overall less important than the crystal movements. Furthermore, in the limiting case of serial microcrystallography every crystal yields single diffraction frame with essentially random orientation. To resolve such cases different approaches have been developed (Campbell, 1995, Helliwell *et al.*, 1989, Ren *et al.*, 1999, Gevorkov *et al.*, 2020, Gevorkov *et al.*, 2019, Beyerlein *et al.*, 2017, Ginn *et al.*, 2016), whereas our method is not applicable.

3. Conclusions and summary

A new algorithm to refine the diffractometer instrument model using normalised reciprocal space vectors has been developed and tested for use in the analysis of synchrotron-generated X-ray Laue diffraction data. The method is applicable for data sets in which multiple consecutive frames are recorded for different crystal orientations and no irregular sample movements are present. The method does not need any data other than the diffraction spot positions and frame angular setting angles. As it has been proved for both model simulated and experimental data sets, the method provides very good results. The refinement readily converges even when the initial deviations from the target values are rather large. Most importantly, the method allows for determination of the IM parameters which had been previously unknown or had been known with low accuracy (which significantly hampered the orientation matrix determination). This constitutes a major improvement in the small-molecule X-ray Laue diffraction processing pipeline. The algorithm is implemented in our new Laue data processing software (Szarejko *et al.*, 2020, Jarzembska *et al.*, 2019). The current version of the program (including the source code), interfaced also with the *LAUEUTIL* suite (Kalinowski *et al.*, 2011, Kalinowski *et al.*, 2012), is available from the authors upon request (the program code will be available publicly open-source shortly).

Acknowledgements

R.K., D.S. and P.Ł. would like to thank the SONATA grant (2016/21/D/ST4/03753) of the National Science Centre in Poland for financial support. L.E.H. and P.R.R. are grateful to the Engineering and Physical Sciences Research Council (UK) for funding (grant No. EP/K004956/1). Some of the time-resolved X-ray diffraction experiments were performed at the ID09 beamline of the European Synchrotron Radiation Facility (ESRF), Grenoble, France.

The research used also the resources of the Advanced Photon Source (APS), a US Department of Energy (DOE) Office of Science User Facility operated for the DOE Office of Science by Argonne National Laboratory under contract No. DE-AC02-06CH11357. Use of BioCARS was additionally supported by the National Institute of General Medical Sciences of the National Institutes of Health (NIH) under grant No. R24GM111072 (note: the content is solely the responsibility of the authors and does not necessarily represent the official views of NIH). Time-resolved set-up at Sector 14 was funded in part through collaboration with Philip Anfinrud (NIH/NIDDK). Authors thank Robert Henning, Anthony DiChiara and Vukica Šrajer for continuous support of our APS experiments.

Associated content

Supporting information:

The Supporting Information is available free of charge and contains definitions of all parameters indispensable to describe the Laue diffraction geometry and the instrument model together with equations needed for least-squares refinement. It also contains all information about simulation of the Laue data sets, as well as example frames of both simulated and experimental data sets.

Author information

Corresponding authors:

Radosław Kamiński (rkaminski85@uw.edu.pl)

Katarzyna N. Jarzembska (katarzyna.jarzembska@uw.edu.pl)

ORCID:

Radosław Kamiński: 0000-0002-8450-0955

Dariusz Szarejko: 0000-0003-2624-5551

Martin N. Pedersen: 0000-0001-6975-5071

Lauren E. Hatcher: 0000-0002-1549-9727

Piotr Łaski: 0000-0002-6410-5587

Paul R. Raithby: 0000-0002-2944-0662

Michael Wulff: 0000-0003-3784-9019

Katarzyna N. Jarzembska: 0000-0003-4026-1849

Notes:

The authors declare no competing financial interest.

References

Arvai, A. (2019). *Adxv - A program to display X-Ray diffraction images.*

Benedict, J. B., Makal, A., Sokolow, J. D., Trzop, E., Scheins, S., Henning, R., Graber, T. & Coppens, P. (2011). *Chem. Commun.* **47**, 1704-1706.

Beyerlein, K. R., White, T. A., Yefanov, O., Gati, C., Kazantsev, I. G., Nielsen, N. F.-G., Larsen, P. M., Chapman, H. N. & Schmidt, S. (2017). *J. Appl. Cryst.* **50**, 1075-1083.

Borgstahl, G. E. O., Williams, D. R. & Getzoff, E. D. (1995). *Biochemistry* **34**, 6278-6287.

Busing, W. R. & Levy, H. A. (1967). *Acta Cryst.* **22**, 457-464.

Campbell, J. W. (1995). *J. Appl. Cryst.* **28**, 228-236.

Coppens, P. (2011). *J. Phys. Chem. Lett.* **2**, 616-621.

Coppens, P. & Fournier, B. (2015). *J. Synchrotron Rad.* **22**, 280-287.

Coppens, P., Kamiński, R. & Schmøkel, M. S. (2010). *Acta Cryst. Sect. A* **66**, 626-628.

Coppens, P., Makal, A., Fournier, B., Jarzembska, K. N., Kamiński, R., Basuroy, K. & Trzop, E. (2017). *Acta Cryst. Sect. B* **73**, 23-26.

Coppens, P., Pitak, M., Gembicky, M., Messerschmidt, M., Scheins, S., Benedict, J. B., Adachi, S.-I., Sato, T., Nozawa, S., Ichiyanagi, K., Chollet, M. & Koshihara, S.-Y. (2009). *J. Synchrotron Rad.* **16**, 226-230.

Coppens, P., Zhang, L., Thomas, R., Chen, Y., Jarzembska, K., Kaminski, R., Trzop, E. & Fournier, B. (2016). *Phys. Scr.* **91**, 023003.

Cruickshank, D. W. J., Helliwell, J. R. & Moffat, K. (1987). *Acta Cryst. Sect. A* **43**, 656-674.

Cruickshank, D. W. J., Helliwell, J. R. & Moffat, K. (1991). *Acta Cryst. Sect. A* **47**, 352-373.

Einspahr, H., Parkst, E. H., Sugunall, K., Subramanianll, E. & Suddath, F. L. (1986). *J. Biol. Chem.* **261**, 16518-16527.

Gevorkov, Y., Barty, A., Brehm, W., White, T. A., Tolstikova, A., Wiedorn, M. O., Meents, A., Grigat, R.-R., Chapman, H. N. & Yefanov, O. (2020). *Acta Cryst. Sect. A* **76**, 121-131.

Gevorkov, Y., Yefanov, O., Barty, A., White, T. A., Mariani, V., Brehm, W., Tolstikova, A., Grigat, R.-R. & Chapman, H. N. (2019). *Acta Cryst. Sect. A* **75**, 694-704.

Ginn, H. M., Roedig, P., Kuo, A., Evans, G., Sauter, N. K., Ernst, O. P., Meents, A., Mueller-Werkmeister, H., Miller, R. J. D. & Stuart, D. I. (2016). *Acta Cryst. Sect. D* **72**, 956-965.

Graber, T., Anderson, S., Brewer, H., Chen, Y.-S., Cho, H., Dashdorj, N., Henning, R. W., Kosheleva, I., Macha, G., Meron, M., Pahl, R., Ren, Z., Ruan, S., Schotte, F., Šrajer, V., Viccaro, P. J., Westferro, F., Anfinrud, P. & Moffat, K. (2011). *J. Synchrotron Rad.* **18**, 658-670.

Hajdu, J., Machin, P. A., Campbell, J. W., Greenhough, T. J., Clifton, I. J., Zurek, S., Gover, S., Johnson, L. N. & Elder, M. (1987). *Nature* **329**, 178.

Hatcher, L. E. & Raithby, P. R. (2014). *Coord. Chem. Rev.* **277-278**, 69-79.

Helliwell, J. R., Habash, J., Cruickshank, D. W. J., Harding, M. M., Greenhough, T. J., Campbell, J. W., Clifton, I. J., Elder, M., Machin, P. A., Papiz, M. Z. & Zurek, S. (1989). *J. Appl. Cryst.* **22**, 483-497.

Jarzembska, K. N., Hapka, M., Kamiński, R., Bury, W., Kutniewska, S. E., Szarejko, D. & Szczęśniak, M. M. (2019). *Crystals* **9**, 36.

Jarzembska, K. N., Kamiński, R., Dziubek, K. F., Citroni, M., Paliwoda, D., Durka, K., Fanetti, S. & Bini, R. (2018). *Inorg. Chem.* **57**, 8509-8520.

Jarzembska, K. N., Kamiński, R., Fournier, B., Trzop, E., Sokolow, J. D., Henning, R., Chen, Y. & Coppens, P. (2014). *Inorg. Chem.* **53**, 10594-10601.

Kalinowski, J. A., Fournier, B., Makal, A. & Coppens, P. (2012). *J. Synchrotron Rad.* **19**, 637-646.

Kalinowski, J. A., Makal, A. & Coppens, P. (2011). *J. Appl. Cryst.* **44**, 1182-1189.

Kaminski, R., Benedict, J., Trzop, E., Jarzembska, K., Fournier, B. & Coppens, P. (2014). *Acta Cryst. Sect. A* **70**, C775.

Koshevoy, I. O., Shakirova, J. R., Melnikov, A. S., Haukka, M., Tunik, S. P. & Pakkanena, T. A. (2011). *Dalton Trans.* **40**, 7927-7933.

Machin, P. (1985). Laue photographs using Synchrotron x-radiation. Report on a Daresbury Synchrotron Radiation PX users meeting and additions of work done since then Vol. 15, CCP4 Newsletter on Protein Crystallography.

Makal, A., Benedict, J., Trzop, E., Sokolow, J., Fournier, B., Chen, Y., Kalinowski, J. A., Graber, T., Henning, R. & Coppens, P. (2012). *J. Phys. Chem. A* **116**, 3359-3365.

Paciorek, W. A., Meyer, M. & Chapuis, G. (1999). *Acta Cryst.* **A55**, 543-557.

Ren, Z., Bourgeois, D., Helliwell, J. R., Moffat, K., Šrajer, V. & Stoddard, B. L. (1999). *J. Synchrotron Rad.* **6**, 891-917.

Schotte, F., Cho, H. S., Kaila, V. R. I., Kamikubo, H., Dashdorj, N., Henry, E. R., Graber, T. J., Henning, R., Wulff, M., Hummer, G., Kataoka, M. & Anfinru, P. A. (2012). *Proc. Natl. Acad. Sci. U.S.A.* **109**, 19256-19261.

Šrajer, V., Crosson, S., Schmidt, M., Key, J., Schotte, F., Anderson, S., Perman, B., Ren, Z., Teng, T.-Y., Bourgeois, D., Wulff, M. & Moffat, K. (2000). *J. Synchrotron Rad.* **7**, 236-244.

Szarejko, D., Kamiński, R., Łaski, P. & Jarzembska, K. N. (2020). *J. Synchrotron Rad.* **27**, 405-413.

Trzop, E., Fournier, B., Jarzembska, K., Sokolow, J., Kaminski, R., Benedict, J., Chen, Y., Henning, R. & Coppens, P. (2014). *Acta Cryst. Sect. A* **70**, C776.

Vorontsov, I., Pillet, S., Kamiński, R., Schmøkel, M. S. & Coppens, P. (2010). *J. Appl. Cryst.* **43**, 1129-1130.

Vorontsov, I. I., Graber, T., Kovalevsky, A. Y., Novozhilova, I. V., Gembicky, M., Chen, Y.-S. & Coppens, P. (2009). *J. Am. Chem. Soc.* **131**, 6566-6573.

Wulff, M., Plech, A., Eybert, L., Randler, R., Schotte, F. & Anfinrud, P. (2002). *Farad. Discuss.* **122**, 13-26.

SUPPORTING INFORMATION

Instrument-model refinement in normalised reciprocal-vector space for X-ray Laue diffraction

Radosław Kamiński,[a,*] Dariusz Szarejko,[a] Martin N. Pedersen,[b] Lauren E. Hatcher,[c,d] Piotr Łaski,[a] Paul R. Raithby,[c] Michael Wulff,[e] Katarzyna N. Jarzembska [a,*]

[a] Department of Chemistry, University of Warsaw, Żwirki i Wigury 101, 02-089 Warsaw, Poland

[b] Niels Bohr Institute, University of Copenhagen, Universitetsparken 5, 2100 Copenhagen, Denmark

[c] Department of Chemistry, University of Bath, Claverton Down, Bath, BA2 7AY, United Kingdom

[d] School of Chemistry, Cardiff University, Main Building, Park Place, Cardiff, CF10 3AT, United Kingdom

[e] European Synchrotron Radiation Facility, 71 avenue des Martyrs, 38043 Grenoble, France

* Corresponding authors: Radosław Kamiński (rkaminski85@uw.edu.pl)
Katarzyna N. Jarzembska (katarzyna.jarzembska@uw.edu.pl)

1S. Instrument model and refinement details

Matrix notation for vectors is used; $\mathbf{a}^{\mathrm{T}}$ stands for a transpose of the matrix $\mathbf{a}$; scalar product in Cartesian basis is $\mathbf{a} \cdot \mathbf{b} = \mathbf{a}^{\mathrm{T}}\mathbf{b}$; for clarity in the text column vectors are written as rows, *i.e.* $[a_1 \quad a_2 \quad \ldots]^{\mathrm{T}}$. When needed the coordinate system is added in the subscript (*i.e.* $[\cdot]_S$ is matrix of vector components in coordinate system S). Laboratory coordinate system $L = (\mathbf{e}_x, \mathbf{e}_y, \mathbf{e}_z)$ is placed in the ideal goniometer centre (X axis along X-ray beam, Z vertical to the top). Primary X-ray beam position is assumed to be fixed along the X axis (*i.e.* along the $\mathbf{e}_x$ vector): $\mathbf{s}_0 = \mathbf{e}_x = [1 \quad 0 \quad 0]_L^{\mathrm{T}}$. Detector coordinate system $D_0 = (\mathbf{d}_x, \mathbf{d}_y, \mathbf{d}_z)$ is anchored in the detector centre (X axis horizontal, Y vertical). Spot position expressed in D_0 is described as vector $\mathbf{r} = [x \quad y \quad 0]_{D_0}^{\mathrm{T}}$, whereas the position of the point where the primary beam hits the detector is $\mathbf{r}_0 = [x_0 \quad y_0 \quad 0]_{D_0}^{\mathrm{T}}$. Position of the spot in respect to the primary beam position is $\Delta\mathbf{r} = \mathbf{r} - \mathbf{r}_0 = [x - x_0 \quad y - y_0 \quad 0]_{D_0}^{\mathrm{T}}$. Calculation of normalised $\underset{\sim}{\mathbf{h}}$ in L is obtained by the following formulas:

$$\mathbf{x} = d \cdot \mathbf{s}_0 + \Delta\mathbf{r} = \begin{bmatrix} d \\ -(x - x_0) \\ y - y_0 \end{bmatrix}_L \tag{S1}$$

$$\mathbf{s} = \frac{\mathbf{x}}{\|\mathbf{x}\|} \quad , \quad \mathbf{y} = \mathbf{s} - \mathbf{s}_0 \quad , \quad \underset{\sim}{\mathbf{h}} = \frac{\mathbf{y}}{\|\mathbf{y}\|} \tag{S2}$$

where $\|\cdot\|$ is the vector norm. See Figure 1S for visualisation of respective vectors and coordinate systems. Finally, vector $\underset{\sim}{\mathbf{h}}$ rotated to the goniometer-head-fixed coordinate system $G = (\mathbf{g}_x, \mathbf{g}_y, \mathbf{g}_z)$ is obtained by application of the rotation matrix $\mathbf{R}$, different for each frame: $\underset{\sim}{\mathbf{h}}_0 = \mathbf{R}^{\mathrm{T}}\underset{\sim}{\mathbf{h}}$ (where $\mathbf{R}^{-1} = \mathbf{R}^{\mathrm{T}}$). Note that G and L coordinate systems overlay for all goniometer angles set to zero.

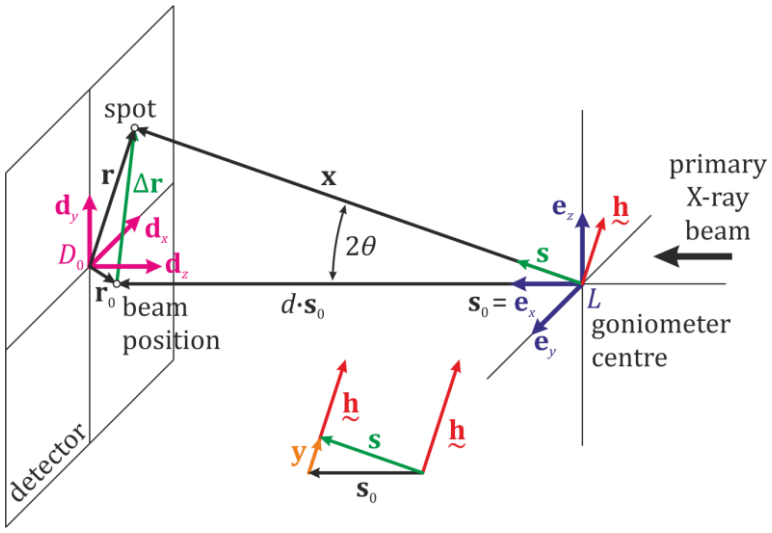

Figure 1S. Detector and laboratory coordinate systems, $D_0 = (\mathbf{d}_x, \mathbf{d}_y, \mathbf{d}_z)$ and $L = (\mathbf{e}_x, \mathbf{e}_y, \mathbf{e}_z)$, and vectors needed in the calculations.

Native ('raw') spot position on the detector is expressed in $D_2 = (\mathbf{i}, \mathbf{j}, \mathbf{k})$ pixel-based coordinate system anchored in the centre of the top left detector pixel (right-handed, $\mathbf{i}$ points down, $\mathbf{j}$ right); this is a basic definition used in majority of image processing applications. We introduce real-valued coordinate system $D_1 = (\boldsymbol{\delta}_x, \boldsymbol{\delta}_y, \boldsymbol{\delta}_z)$ centred on top left detector corner (orientation the same as for D_2). Relations of spot coordinates in D_0 and these two coordinate systems are expressed by the following formulas:

$$\begin{bmatrix} x \\ y \\ 0 \end{bmatrix}_{D_0} = \begin{bmatrix} x_\delta - \frac{1}{2}p_\mathrm{h}n_\mathrm{h} \\ \frac{1}{2}p_\mathrm{v}n_\mathrm{v} - y_\delta \\ 0 \end{bmatrix}_{D_1} = \begin{bmatrix} j + \frac{1}{2}p_\mathrm{h}(1 - n_\mathrm{h}) \\ \frac{1}{2}p_\mathrm{v}(n_\mathrm{v} - 1) - i \\ 0 \end{bmatrix}_{D_2} \tag{S3}$$

where n_h and n_v are number of detector pixels, and p_h and p_v are pixel sizes, for horizontal and vertical directions, respectively.

To perform a least-squares minimisation the derivatives of the norm of the difference of two computed $\underset{\sim}{\mathbf{h}}_0$ vectors for the same spot appearing for two consecutive frames (*i.e.* $\Delta\underset{\sim}{\mathbf{h}}_{0,k,j} = \underset{\sim}{\mathbf{h}}_{0,k,j} - \underset{\sim}{\mathbf{h}}_{0,k,j+1}$) are needed. The derivatives are computed as follows:

$$\frac{\partial}{\partial p}\left\|\Delta\underset{\sim}{\mathbf{h}}_{0,k,j}\right\| = \frac{\Delta\underset{\sim}{\mathbf{h}}_{0,k,j}^{T}}{\left\|\Delta\underset{\sim}{\mathbf{h}}_{0,k,j}\right\|}\left(\frac{\partial}{\partial p}\underset{\sim}{\mathbf{h}}_{0,k,j} - \frac{\partial}{\partial p}\underset{\sim}{\mathbf{h}}_{0,k,j+1}\right) \tag{S4}$$

where $\underset{\sim}{\mathbf{h}}_{0,k,j}$ is vector for the k-pair of $\underset{\sim}{\mathbf{h}}_0$ vectors matched for frames j and $j+1$; p is selected refined parameter. Accordingly (for clarity we drop indexes k and j; note matrices $\mathbf{R}$ depend on frame index j):

$$\frac{\partial}{\partial p}\underset{\sim}{\mathbf{h}}_0 = \mathbf{R}^{\mathrm{T}}\left(\frac{1}{\|\mathbf{y}\|}\left(\frac{\partial\mathbf{y}}{\partial p}\right) - \frac{\mathbf{y}}{\|\mathbf{y}\|^3}\left[\mathbf{y}^{\mathrm{T}}\left(\frac{\partial\mathbf{y}}{\partial p}\right)\right]\right) \tag{S5}$$

$$\frac{\partial\mathbf{y}}{\partial p} = \frac{1}{\|\mathbf{x}\|}\left(\frac{\partial\mathbf{x}}{\partial p}\right) - \frac{\mathbf{x}}{\|\mathbf{x}\|^3}\left[\mathbf{x}^{\mathrm{T}}\left(\frac{\partial\mathbf{x}}{\partial p}\right)\right] \tag{S6}$$

Since $\mathbf{x} = [d \quad -(x-x_0) \quad y-y_0]_L^{\mathrm{T}}$ its derivatives simply equal to:

$$\frac{\partial\mathbf{x}}{\partial d} = \begin{bmatrix}1\\0\\0\end{bmatrix}_L \quad , \quad \frac{\partial\mathbf{x}}{\partial x_0} = \begin{bmatrix}0\\1\\0\end{bmatrix}_L \quad , \quad \frac{\partial\mathbf{x}}{\partial y_0} = \begin{bmatrix}0\\0\\-1\end{bmatrix}_L \tag{S7}$$

Please note the actual implementation of the procedure works in native detector pixel coordinates, as denoted above in the equation S3. Therefore, inside the program source code the last component of the third derivative in S7 (*i.e.* $\partial\mathbf{x}/\partial y_0$) is in fact positive.

Reflections from two consecutive frames j and $j+1$ are considered to form a pair k when the simple geometrical criterion,

$$\arccos\left(\underset{\sim}{\mathbf{h}}_{0,k,j}^{\mathrm{T}}\underset{\sim}{\mathbf{h}}_{0,k,j+1}\right) = \theta \le \theta_0 \tag{S8}$$

is fulfilled, where θ_0 is the specified threshold (note here both vectors are of unit length, thus obviously $\left\|\underset{\sim}{\mathbf{h}}_{0,k,j}\right\| \cdot \left\|\underset{\sim}{\mathbf{h}}_{0,k,j+1}\right\| = 1$).

2S. Simulation of X-ray Laue patterns

Instrument model used in simulations is more general, which provides more flexibility for future applications. In addition to coordinate systems L and G, presented in the previous section, we define also extra coordinate systems $K^* = (\mathbf{a}^*, \mathbf{b}^*, \mathbf{c}^*)$ (non-Cartesian reciprocal crystal coordinate system) and $C = (\mathbf{c}_x, \mathbf{c}_y, \mathbf{c}_z)$ (introduced to easily decompose the orientation matrix into 'orientation' and 'unit-cell shape' parts). The transformation between K^* and C systems is defined with the following matrix $\mathbf{B}$ (expressed in reciprocal lattice unit cell parameters):

$$\mathbf{B} = \begin{bmatrix} a^* & 0 & 0 \\ b^*\cos(\gamma^*) & b^*\sin(\gamma^*) & 0 \\ c^*\cos(\beta^*) & c^*\dfrac{\cos(\alpha^*)-\cos(\gamma^*)\cos(\beta^*)}{\sin(\gamma^*)} & c^*\left[1-\cos(\beta^*)-\dfrac{\cos(\alpha^*)-\cos(\gamma^*)\cos(\beta^*)}{\sin(\gamma^*)}\right] \end{bmatrix} \tag{S9}$$

where the transformation takes the form:

$$\mathbf{h}_C = \mathbf{B}^{\mathrm{T}} \cdot \mathbf{h}_{K^*} \tag{S10}$$

in which $\mathbf{h} = h\mathbf{a}^* + k\mathbf{b}^* + l\mathbf{c}^* = x_{\mathrm{c}}\mathbf{c}_x + y_{\mathrm{c}}\mathbf{c}_y + z_{\mathrm{c}}\mathbf{c}_z$. The relationship between K^* and C frames is depicted in Figure 2S.

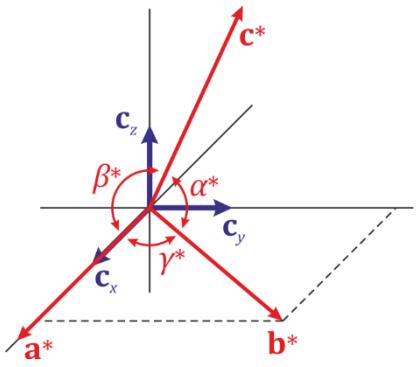

Figure 2S. Relationship between $C = (\mathbf{c}_x, \mathbf{c}_y, \mathbf{c}_z)$ and $K^* = (\mathbf{a}^*, \mathbf{b}^*, \mathbf{c}^*)$ coordinate systems. Vector $\mathbf{a}^*$ is along $\mathbf{c}_x$, and $\mathbf{b}^*$ lies in the plane formed by $\mathbf{c}_x$ and $\mathbf{c}_y$ vectors.

For computational purposes the matrix **B** is expressed in direct lattice unit-cell parameters using the very well-known formulas:

$$a^* = \frac{bc\sin\alpha}{V} \qquad b^* = \frac{ac\sin\beta}{V} \qquad c^* = \frac{ab\sin\gamma}{V}$$
$$\cos(\alpha^*) = \frac{\cos\beta\cos\gamma - \cos\alpha}{\sin\beta\sin\gamma} \qquad \cos(\beta^*) = \frac{\cos\alpha\cos\gamma - \cos\beta}{\sin\alpha\sin\gamma} \qquad \cos(\gamma^*) = \frac{\cos\alpha\cos\beta - \cos\gamma}{\sin\alpha\sin\beta} \tag{S11}$$
$$\sin(\gamma^*) = \frac{V}{abc\sin\alpha\sin\beta} \qquad V = abc\sqrt{1-\cos^2\alpha-\cos^2\beta-\cos^2\gamma+2\cos\alpha\cos\beta\cos\gamma}$$

Orientation matrix **U** describes how the crystal reciprocal axes are related to the goniometer-head-fixed coordinate system (*i.e.* relation between K^* and G coordinate systems). We define the matrix **U** as follows:

$$\mathbf{h}_G = \mathbf{U} \cdot \mathbf{h}_{K^*} \tag{S12}$$

where for any vector we have $\mathbf{h} = h\mathbf{a}^* + k\mathbf{b}^* + l\mathbf{c}^* = x_{\mathrm{g}}\mathbf{g}_x + y_{\mathrm{g}}\mathbf{g}_y + z_{\mathrm{g}}\mathbf{g}_z$. This definition is identical to the one used by Kalinowski *et al.* (Kalinowski *et al.*, 2011) and closely related to the definitions used in the seminal paper by Busing & Levy (Busing & Levy, 1967). The relation between G and C coordinate systems (both are Cartesian) is then expressed with matrix **C** as follows:

$$\mathbf{h}_G = \mathbf{C}^{\mathrm{T}} \cdot \mathbf{h}_C \tag{S13}$$

From this definition it follows that $\mathbf{h}_G = \mathbf{C}^{\mathrm{T}}\mathbf{B}^{\mathrm{T}} \cdot \mathbf{h}_{K^*} = (\mathbf{BC})^{\mathrm{T}} \cdot \mathbf{h}_{K^*}$. Rotation matrix $\mathbf{C}$ is expressed via Euler angles (θ_1, θ_2 and θ_3) in the following way:

$$\mathbf{C} = \mathbf{R}_1(\theta_1) \cdot \mathbf{R}_2(\theta_2) \cdot \mathbf{R}_3(\theta_3) \tag{S14}$$

where

$$\mathbf{R}_1(\theta_1) = \begin{bmatrix} \cos(\theta_1) & -\sin(\theta_1) & 0 \\ \sin(\theta_1) & \cos(\theta_1) & 0 \\ 0 & 0 & 1 \end{bmatrix} \quad \mathbf{R}_2(\theta_2) = \begin{bmatrix} 1 & 0 & 0 \\ 0 & \cos(\theta_2) & -\sin(\theta_2) \\ 0 & \sin(\theta_2) & \cos(\theta_2) \end{bmatrix} \quad \mathbf{R}_3(\theta_3) = \begin{bmatrix} \cos(\theta_3) & -\sin(\theta_3) & 0 \\ \sin(\theta_3) & \cos(\theta_3) & 0 \\ 0 & 0 & 1 \end{bmatrix} \tag{S15}$$

Finally, every crystal is appropriately rotated on the goniometer. We assume all rotations of the goniometer are defined as counter-clockwise. When the goniometer angles are rotated, the selected **h** vector is rotated alongside with the goniometer-head-fixed coordinate system G (*i.e.* vector **h** coordinates in G remain constant). General scheme of the Euler-type goniometer is presented in Figure 3S. We introduce two other Cartesian coordinate systems associated with ω and χ circles: $O = (\mathbf{o}_x, \mathbf{o}_y, \mathbf{o}_z)$ and $M = (\mathbf{m}_x, \mathbf{m}_y, \mathbf{m}_z)$. We note when all seting angles are zero the G, O and M coordinate systems overlay with L. We now systematically define all counter-clockwise rotations along ω, χ and ϕ axes (the same symbols are used for respective angles) as:

$$\mathbf{h}_L = \mathbf{R}_z(\omega) \cdot \mathbf{h}_O \tag{S16}$$

$$\mathbf{h}_O = \mathbf{R}_x(\chi) \cdot \mathbf{h}_M \tag{S17}$$

$$\mathbf{h}_M = \mathbf{R}_z(\phi) \cdot \mathbf{h}_G \tag{S18}$$

This, finally, yields a total rotation as:

$$\mathbf{h}_L = \mathbf{R} \cdot \mathbf{h}_G \tag{S19}$$

where the matrix **R** takes the form:

$$\mathbf{R} = \mathbf{R}_z(\omega) \cdot \mathbf{R}_x(\chi) \cdot \mathbf{R}_z(\phi) \tag{S20}$$

and

$$\mathbf{R}_z(\omega) = \begin{bmatrix} \cos\omega & -\sin\omega & 0 \\ \sin\omega & \cos\omega & 0 \\ 0 & 0 & 1 \end{bmatrix} \quad \mathbf{R}_x(\chi) = \begin{bmatrix} 1 & 0 & 0 \\ 0 & \cos\chi & -\sin\chi \\ 0 & \sin\chi & \cos\chi \end{bmatrix} \quad \mathbf{R}_z(\phi) = \begin{bmatrix} \cos\phi & -\sin\phi & 0 \\ \sin\phi & \cos\phi & 0 \\ 0 & 0 & 1 \end{bmatrix} \tag{S21}$$

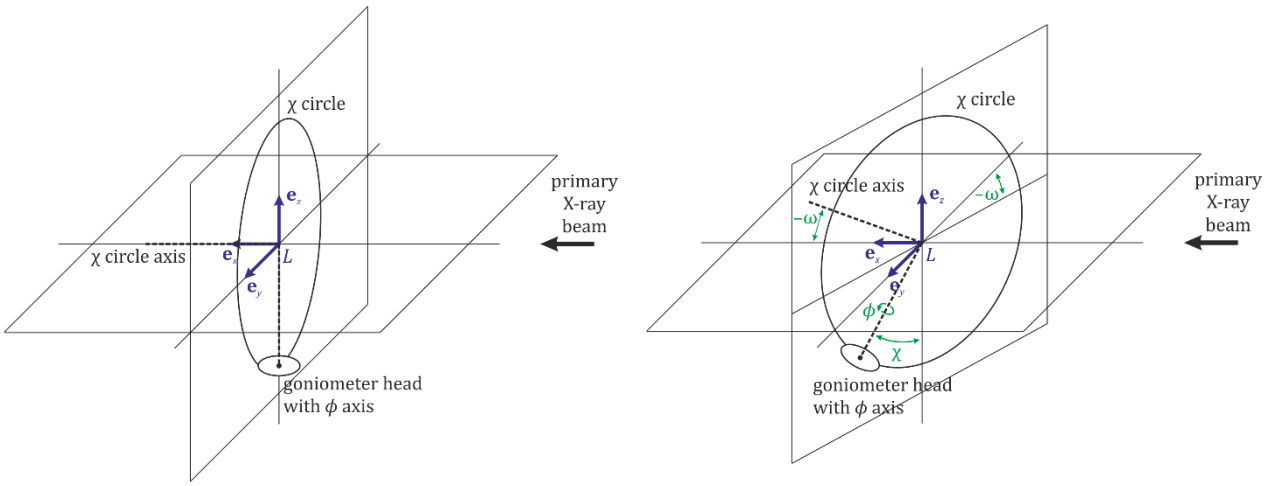

(a) (b)

Figure 3S. Schematic representation of the 4-circle Euler-type goniometer. (a) The instrument with all angles set to zero. (b) Instrument with all angles departed from zero position (all rotations are defined as positive then counter-clockwise; for clarity of the figure the ω is shown as negative).

Finally, the equation allowing to compute the coordinates of vector $\mathbf{h}$ in laboratory frame L given all the matrices and transformation is as follows:

$$\mathbf{h}_L = \mathbf{R} \cdot \mathbf{h}_G = \mathbf{R} \cdot (\mathbf{BC})^{\mathrm{T}} \cdot \mathbf{h}_{K^*} \tag{S22}$$

Where we introduced vector $\mathbf{h}_0 = \mathbf{h}_G = (\mathbf{BC})^{\mathrm{T}}\mathbf{h}_{K^*}$ (*i.e.* vector $\mathbf{h}$ before goniometer rotation angles applied, as in the previous section; notation $\mathbf{h}_0$ is used in the main text for convenience).

For Laue diffraction every spot falling into the region between two extreme Ewald spheres is recorded. For each $\mathbf{h}$ vector its wavelength is calculated using a well-known formula:

$$\lambda = -2\frac{\mathbf{h} \cdot \mathbf{s}_0}{\|\mathbf{h}\|^2} = -2\frac{\mathbf{h} \cdot \mathbf{s}_0}{\mathbf{h} \cdot \mathbf{h}} \tag{S23}$$

The implemented algorithm follows then a simple path:

(i) Generation of the allowed $\mathbf{h}_{K^*}$ vector indices (*i.e.* h, k and l) in reciprocal crystal basis K^*. Limiting values are estimated from the larger Ewald sphere radius ($1/\lambda_{\mathrm{min}}$). Additional $\sin\theta\,/\lambda$ cut-off can be taken into account. At this point the systematic absences can also omitted (not implemented yet).

(ii) Generated $\mathbf{h}_{K^*}$ vectors are transformed to the goniometer-head-fixed Cartesian reference frame of G using the $\mathbf{h}_G = (\mathbf{BC})^{\mathrm{T}}\mathbf{h}_{K^*}$. This set is used in the next steps.

(iii) For every frame (with known frame rotation angles) all $\mathbf{h}_G$ are rotated to the laboratory frame L: $\mathbf{h}_L = \mathbf{R} \cdot \mathbf{h}_0$.

(iv) For each $\mathbf{h}_L$ the wavelength at which the diffraction would occur for this particular vector is computed. At this step we check whether the computed values falls into the region between two limiting Ewald spheres, *i.e.* if $\lambda_{\min} \leq \lambda \leq \lambda_{\max}$. If this is fulfilled the algorithm proceeds further, otherwise the vector is rejected.

(v) Diffraction equation is used to compute the scattering vector $\mathbf{s} = \mathbf{s}_0 + \lambda \cdot \mathbf{h}_L$, and it is checked whether the detector surface intersects the line along this vector (i.e. we check if the spot lies in the detector area). If the last is true, the coordinates of the spot on the detector are computed and saved into the HDF5 file.

(vi) Steps (iii)-(v) are repeated for all frames (a number specified by the user).

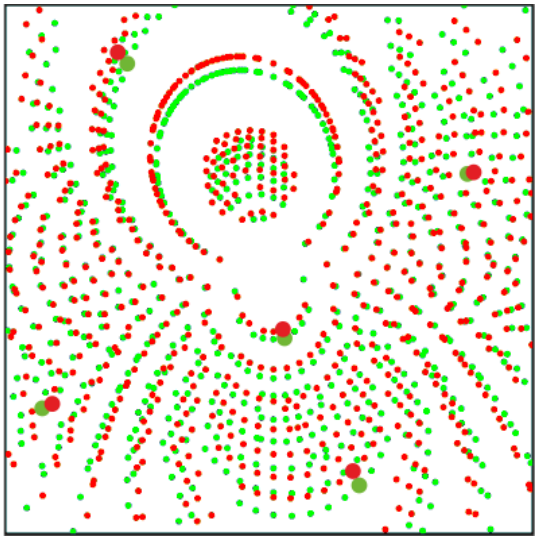

Figure 4S. Overlay of two adjacent frames (angular interval $\Delta\phi$ = 1°) shown for simulated data (silver(I)-copper(I) complex quoted in the main text) – green spots: frame for ϕ = 0°, red spots: frame for ϕ = 1° (crystal horizontal rotation). Large dots represent selected reflections shown in Figure 1*b*.

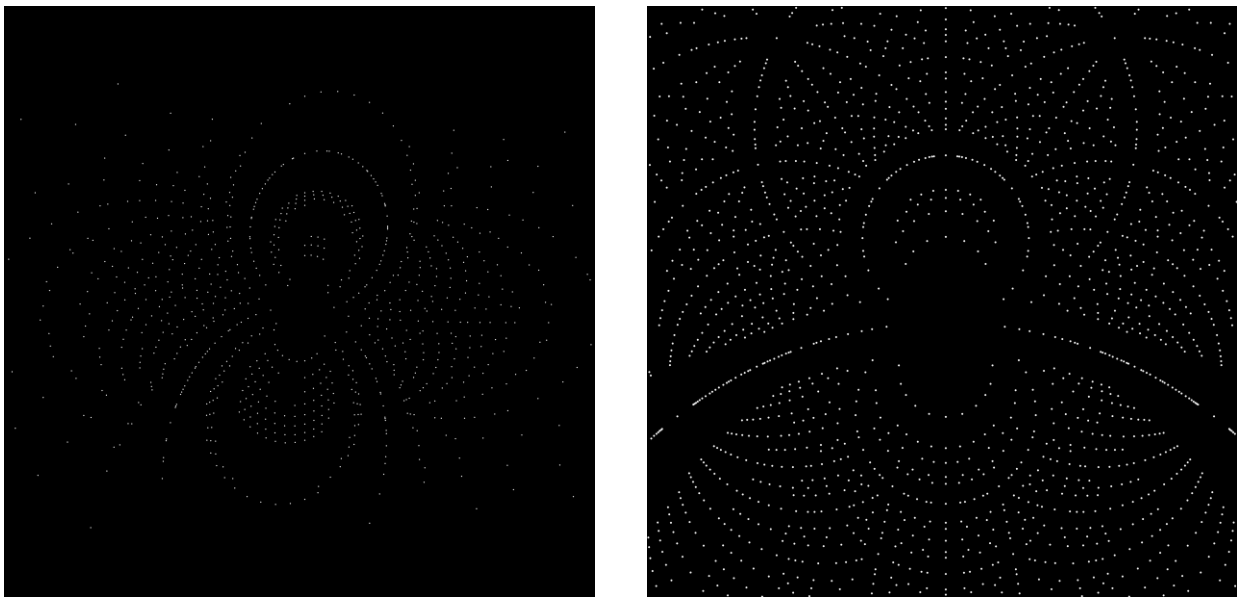

(*a*) (*b*)

Figure 5S. Example simulated frames. (*a*) Single frame generated for the **simAgCu** test sample. (*b*) Single frame generated for the **simPeaL** test sample. For simulation details see Table 1 in the manuscript text.

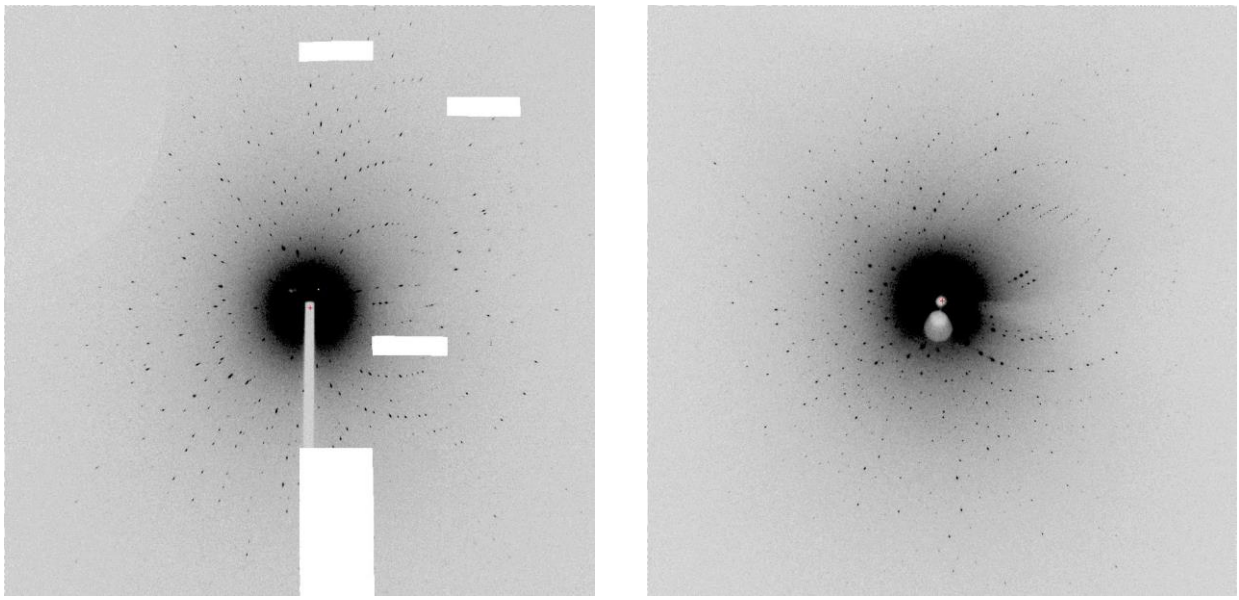

(*a*) (*b*)

Figure 6S. Example experimental frames. (*a*) Single frame recorded at the 14-ID-B beamline at APS for the **expCuDppe** sample (15 keV 'pink' X-ray beam, detector: Rayonix MX340-HS, detector distance: 100 mm, note some unusable detector areas not used in processing). (*b*) Single frame recorded at the ID09 beamline at ESRF for the **expCuDmdpp** sample (15 keV 'pink' X-ray beam, detector: Rayonix MX170-HS, detector distance: 50 mm, note two beamstops are present: the top one – smaller and closer to the detector centre – is for X-rays, and bottom is for the laser beam used in TR experiments).